Advanced Thin Film Core Technology: CIGS Final Technical Report (FTR)

Lorelle Mansfield

National Renewable Energy Laboratory

NREL is a national laboratory of the U.S. Department of Energy
Office of Energy Efficiency & Renewable Energy
Operated by the Alliance for Sustainable Energy, LLC

This report is available at no cost from the National Renewable Energy Laboratory (NREL) at www.nrel.gov/publications.

Contract No. DE-AC36-08GO28308

Technical Report
NREL/TP-5K00-82972
June 2022

Advanced Thin Film Core Technology: CIGS Final Technical Report (FTR)

Lorelle Mansfield

National Renewable Energy Laboratory

Suggested Citation
Mansfield, Lorelle. 2022. *Advanced Thin Film Core Technology: CIGS Final Technical Report (FTR)*. Golden, CO: National Renewable Energy Laboratory. NREL/TP-5K00-82972. https://www.nrel.gov/docs/fy22osti/82972.pdf.

NREL is a national laboratory of the U.S. Department of Energy
Office of Energy Efficiency & Renewable Energy
Operated by the Alliance for Sustainable Energy, LLC

This report is available at no cost from the National Renewable Energy Laboratory (NREL) at www.nrel.gov/publications.

Contract No. DE-AC36-08GO28308

Technical Report
NREL/TP-5K00-82972
June 2022

National Renewable Energy Laboratory
15013 Denver West Parkway
Golden, CO 80401
303-275-3000 • www.nrel.gov

NOTICE

This work was authored by the National Renewable Energy Laboratory, operated by Alliance for Sustainable Energy, LLC, for the U.S. Department of Energy (DOE) under Contract No. DE-AC36-08GO28308. Funding provided by U.S. Department of Energy Office of Energy Efficiency and Renewable Energy Solar Energy Technologies Office. The views expressed herein do not necessarily represent the views of the DOE or the U.S. Government.

Advanced Thin Film Core Technology: CIGS Final Technical Report (FTR)

Agency/Office/Program	DOE/EERE/Solar Energy Technologies Office	
Award Number	DE-EE0034352	
Project Title	Advanced Thin Film Core Technology: CIGS	
Principal Investigator	Lorelle Mansfield, Researcher IV, Lorelle.mansfield@nrel.gov, 303-384-7884	
Business Contact	Dan Friedman, PV Program Manager, Daniel.friedman@nrel.gov, 303-384-6472	
Submission Date	06/08/2022	
DUNS Number	805948051 + 0000	
Recipient Organization	National Renewable Energy Laboratory	
Project Period	**Start:** 10/01/2018	**End:** 3/31/2022
Project Budget	$2,991,432	
Submitting Official Signature	Lorelle M. Mansfield	

Acknowledgement: "This material is based upon work supported by the U.S. Department of Energy's Office of Energy Efficiency and Renewable Energy (EERE) under the Lab Call Award Number 34352."

1. Executive Summary

$Cu(In,Ga)Se_2$ (CIGS) thin-film photovoltaics are a high-efficiency and reliable technology. This project completed research in two important areas and was designed to work collaboratively with industrial partners. Task 1: Alkali Science focused on alkali post-deposition treatments (PDT). PDTs have been instrumental in the dramatic voltage improvements that have moved CIGS device efficiencies from 20% to 23.35% [1]. Based on a survey of CIGS companies at the beginning of the project, the single biggest breakthrough for the CIGS community would be a mechanistic understanding of the role of alkalis in the material system. Significant accomplishments of Task 1: Alkali Science are listed below.

- KF post-deposition treatments were shown to improve lifetime, open-circuit voltage (V_{OC}), and efficiency of industrial partner samples, even when done as a later step, separate from the original CIGS deposition.
- KF boosted efficiency when incorporated at the end of the third stage of NREL CIGS growth.
- XPS characterization of CIGS surfaces with and without PDTs led to a proposed mechanism whereby K drives structural transformation at 350 °C that is locked in at room temperature even after K is rinsed away.
- Published recipes for KF and RbF PDTs. Literature to date did not provide enough detail to quickly reproduce experimental results.
- Identified most important parameters (RbF cell temperature and lamp setpoint temperature) and set boundaries for successful RbF PDTs.

The purpose of Task 2: Cell-level Reliability was to overcome the largest challenges to investor confidence and long product lifetime in CIGS-based photovoltaic products: metastability, shading-induced hot spots, and potential-induced degradation (PID). Key findings were made in each of these areas by studying CIGS reliability at the cell level.

- Published NREL's cell-level reliability testing procedures along with challenges that were encountered while developing them. These were also distributed to the community through an MRS conference presentation.
- Decreased metastability by adding a CdS hole-injection layer between the CIGS and Zn(O,S) in the device stack. It also improved device performance. Materials other than CdS can be used for the same purpose.
- Reduced front-glass PID by replacing soda-lime glass with low-Na borosilicate glass.
- Found that PID depends on leakage current and light/electrical bias. This will help labs avoid test-specific degradation.
- Discovered that CIGS can suffer from two different types of PID with different mechanisms. Front is slower and leads to shunting ZnO. Back is faster and degrades the p-n junction.
- Holding cells at open circuit slows PID compared to short circuit. This affects testing protocols for glass/glass modules.

Table of Contents

2. Background

Alkali PDTs have been instrumental in the dramatic voltage improvements that have moved CIGS device efficiencies from 20% to 23.35% [1]. This field has seen significant research in the past several years. Alkali fluorides react with the CIGS surface and alter its chemical composition. In efficient devices, $RbInSe_2$ and $CsInSe_2$ were both directly observed at the surface of CIGS absorbers [2], and hypothesized to passivate dangling bonds through a 3D/2D chalcopyrite/monoclinic interface [3]. Although not directly observed, indirect evidence indicates that $KInSe_2$ also passivates high-efficiency CIGS [4][5][6]. Several reviews of alkali incorporation in CIGS have extensive detail [7][8][9][10].

The largest reliability challenges in CIGS-based photovoltaic products are metastability, shading-induced hot spots, and PID. They are often studied in modules, however cell-level reliability in CIGS has received less attention. A few groups are still interested in metastability [11], [12], often as it relates to post-deposition-treated CIGS. Some study has also continued in reverse-bias damage of CIGS devices [13][14]. Potential-induced degradation is probably the most investigated topic in CIGS reliability, although it is usually discussed in modules [15] rather than cells [16]. Our cell-level reliability procedures have been well-documented to provide guidance for future reliability studies [17].

3. Project Objectives

NREL has a unique capability to study CIGS surfaces without air exposure to gain a fundamental understanding of alkali treatments. Comparisons will be made between alkali co-evaporated with the CIGS absorber and alkali PDTs. Devices fabricated from each process will be evaluated and results will inform us of the best practices for alkali incorporation. NREL PDTs can be applied to industrial stakeholder samples to help guide them to the best implementation for their products.

Testing for reliability earlier in the research cycle increases the probability of avoiding common module reliability problems before cell changes are implemented on a large scale. Cell-level reliability studies can thus lower the rates of module failures in the field and provide confidence to investors that new technologies will perform as advertised. At the end of the last project, Manufacturing and Reliability Science for CIGS Photovoltaics, additional experiments were identified which will lead to further discoveries. Task 2 is a continuation of that work.

Task descriptions are shown in Table 1. Quarterly progress indicators (QPIs) and annual milestones (AMS) are listed in Table 2. Those that were delayed show two end dates in the Planned/Actual End Date column. The first is the planned end date and the second is the actual completion date.

Table 1: Task list with descriptions.

Task #	Task Name: Task Description:
1	**Task Name**: CIGS Alkali Science **Task Description:** Explore the fundamentals of alkali treatments using co-evaporation and PDTs for introducing KF and RbF to CIGS for high-efficiency thin-film solar cells. Focus on questions important to industrial stakeholders as well as the scientific community.
2	**Task Name:** Cell-Level Reliability **Task Description:** Extend cell-level reliability work that was started in FY16-FY18 which focuses on the three main problems with module reliability in CIGS: metastability, reverse-bias degradation, and potential-induced degradation

Table 2: QPI and milestone list.

Year #	Task #	Milestone	Milestone Name/Description	Planned/ Actual End Date	Milestone Type: Annual or Quarterly
1	**1**	**1**	Baseline CIGS deposition process in PDIL tool (6" by 6") that produces 17% efficiency devices as measured by J-V.	12/31/2018 3/31/2019	Quarterly
1	**1**	**2**	CIGS device V_{OC} is increased by 20 mV due to successful implementation of KF PDT.	3/31/2019	Quarterly
1	**2**	**3**	Sentaurus models that predict the differences in reverse-bias behavior (measured J-V curves) between devices with CdS and those with Zn(O,S).	6/30/2019	Quarterly
1	**1**	**4**	Completed study of KF PDT performed on at least one industrial partner's absorbers resulting in a 20 mV V_{OC} improvement and higher device efficiency over similarly processed samples without a KF PDT. Findings will be reported to the company.	9/30/2019	Annual
2	**1**	**1**	KF incorporated into the CIGS absorber during deposition (not PDT) results in the K content greater than or equal to bulk K levels in samples with a successful KF PDT as defined in QPI 1.1.2. Device V_{OC} increased by at least 20 mV along with efficiency increase above similarly processed samples without KF incorporation.	12/31/2019	Quarterly
2	**1**	**2**	Submit paper on XPS investigation of CIGS with KF and/or the device performance improvements	3/31/2020 Project end	Quarterly

Year #	Task #	Milestone	Milestone Name/Description	Planned/ Actual End Date	Milestone Type: Annual or Quarterly
			and comparisons between KF PDT and co-evaporated KF.		
2	**1**	**3**	CIGS device V_{OC} is increased by 20 mV due to successful implementation of RbF PDT.	6/30/2020 6/30/2021	Quarterly
2	**2**	**4**	Increase (by a factor of 2) the time to potential-induced degradation from front-glass-biased configuration.	9/30/2020	Annual
3	**1**	**1**	Demonstrate 30 mV V_{OC} and/or 1.5% efficiency improvement in the samples from at least one industrial partner using any in-situ or post-deposition KF or RbF treatments.	12/31/2020 Not met	Quarterly
3	**1**	**2**	Submit paper on XPS investigation of CIGS with RbF and/or the device performance improvements and comparisons between RbF PDT and co-evaporated RbF.	3/31/2021 Not met	Quarterly
3	**2**	**3**	Report on best practices for testing and measuring cell-level reliability.	6/30/2021	Quarterly
3	**1**	**4**	Final paper on mechanisms and recommendations for optimal approach to improve thin films with alkalis with evaluation of manufacturability submitted to a peer-reviewed journal. Demonstrate at least 2% absolute device efficiency improvement on an industrial partner's absorber using alkalis and document industrial partner feedback.	9/30/2021 Not met	Annual

4. Project Results and Discussion

Results of this project are described below, listed in order of task from the technical work plan.

4.1. Task 1: CIGS Alkali Science

4.1.1. Baseline CIGS deposition process in PDIL tool (QPI 1.1.1)

The PDIL tool (A.K.A. CIGS cluster tool) is a molecular beam epitaxy (MBE) system attached to a central robot. A vacuum chamber pod on wheels can be attached to the system, and a sample can be moved into it without air exposure. The pod can then be detached and wheeled to characterization systems where the sample can again undergo an air-free transfer. We don't know of another laboratory in the world that has this unique capability. The plan was to use it to investigate the chemical composition of the CIGS surface with and without alkali

treatments using XPS analysis. Understanding how the alkali treatments affect the CIGS surface is an ongoing question in the CIGS community.

To perform the novel alkali experiments, a baseline CIGS deposition process in the PDIL tool was required. This was the focus of QPI 1.1.1. In Q1 of the project we were able to bring up the tool – which had not been used regularly for CIGS depositions in about four years – to make samples with over 15% efficiency (dotted line) as shown in Figure 1 (left). Figure 1 (right) shows the improvements made in Q2 when we were able to meet QPI 1.1.1. The graph shows the five best sample pieces; they all have devices with efficiency over 17% (dashed line) without anti-reflective coating.

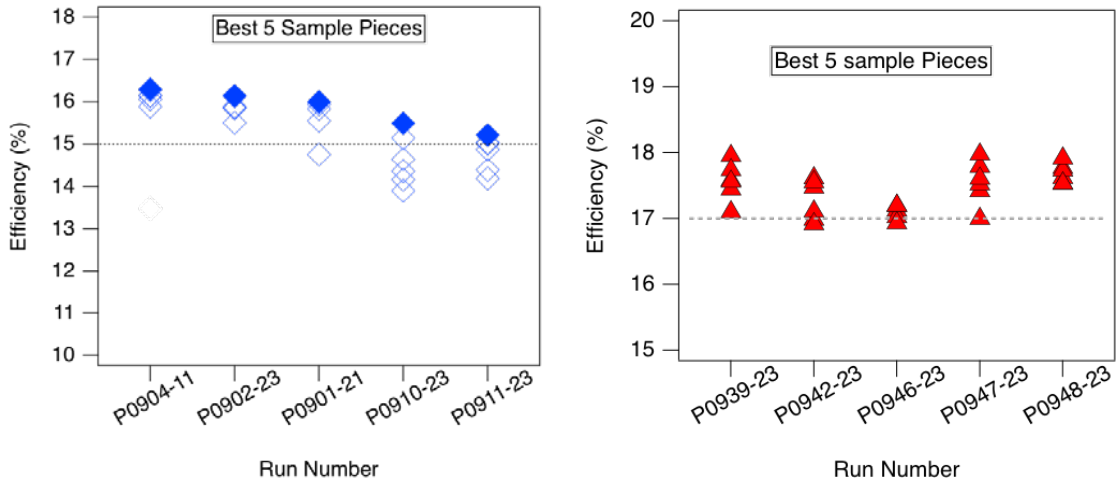

Figure 1. The five best sample pieces in Q1 (left) and in Q2 (right). We were able to improve the efficiencies of PDIL-grown samples from 15-16% to over 17%.

The efficiency increases were achieved by controlling the gallium gradient within the CIGS layer. Figure 2 shows example secondary ion mass spectrometry (SIMS) depth profiles of Ga content through CIGS absorber layers. On the left, run P0902 is compared to M3039, a 20% cell (previous world record), and C3297, a cell with over 17% efficiency. When looking at the SIMS profiles, focus on the shape of the Ga distribution and not the magnitude. The colored dashed lines guide the eye between the surface and the CIGS/Mo interface of the film, at the level of interface Ga. The vertical dotted line is roughly where we wanted the Ga to be the lowest. From the graph we found two things might improve the resulting device efficiency. First, for P0902 (green curve) notice that the Ga is higher at the CIGS surface (near 0 on the bottom axis) than it is at the CIGS/Mo interface near the back of the film. This sets up a situation where carriers can recombine in the depletion region rather than being collected by the front contact as current. The surface Ga content needed to be reduced. Second, the low Ga region is quite narrow in P0902. Solar Frontier widens the low-Ga region, “to mitigate the absorption loss at the long wavelength region,” that can be seen in the quantum efficiency (QE) curve (not shown) [18]. Figure 2 (right) shows how the Ga gradient was improved to get 18% efficiency cells from run P0939 (red). This CIGS film and those with similar profiles produced devices that met QPI 1.1.1, a baseline process to make devices with over 17% efficiency.

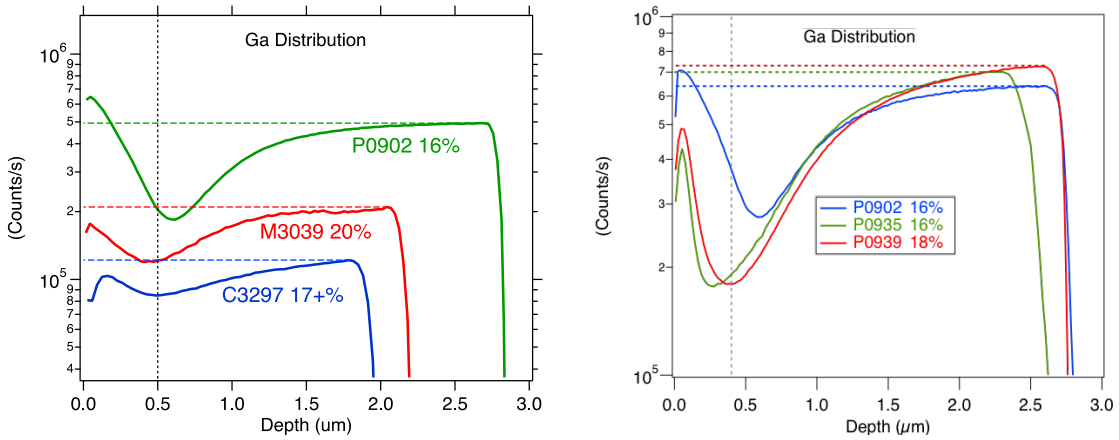

Figure 2. SIMS depth profiles of Ga distribution through the CIGS film thickness. P0902 compared to good runs from our small-area systems (left) and compared to better efficiency samples from the PDIL system (right).

4.1.2. Increase V_{OC} by 20 mV with KF PDT (QPI 1.1.2)

In parallel to dialing in the PDIL recipe, we conducted a designed experiment in the 3" by 3" deposition system to explore the parameter space of the KF post-deposition treatment. We used three factors Lamp Temp, KF Time, and Se Rate with three levels of low, middle, and high values. Plugging these into JMP software design of experiments gave us a matrix of 16 runs to perform. The best conditions for the KF PDT were Lamp Temp = 370°C, KF Time = 6.5 min, and Se Rate = 35 Å/s. This recipe gave us a champion efficiency of over 19% without AR. For QPI 1.1.2, we wanted a recipe that would give us a 20 mV increase in V_{OC} when comparing five standard runs without KF PDT and five KF-PDT runs. Figure 3 shows the results of this experiment. The left graph shows average V_{OC} versus sample number with error bars that represent the standard deviation. The red points on the left half of the graph are standard runs with no KF. Their average V_{OC} of 0.709 V is indicated by the dashed line. Samples with KF PDT on the right side of the graph are shown in blue. The average V_{OC} for these five runs was 0.727 V. This gives the KF-PDT samples an overall increase in V_{OC} of 18 mV over runs with no KF. Figure 3 (right) shows average efficiencies for each of the runs we performed. The standard runs with no KF are red circles on the left side of the graph. They show an average efficiency of 17.6%. The KF-PDT runs on the right are blue triangles, and they have an average efficiency of 18.2%. That is an increase of 0.6% absolute. We did not quite meet the 20 mV increase in V_{OC}, but the strong increase in V_{OC} and efficiency were sufficient to proceed with the KF-PDT experiments on partner samples.

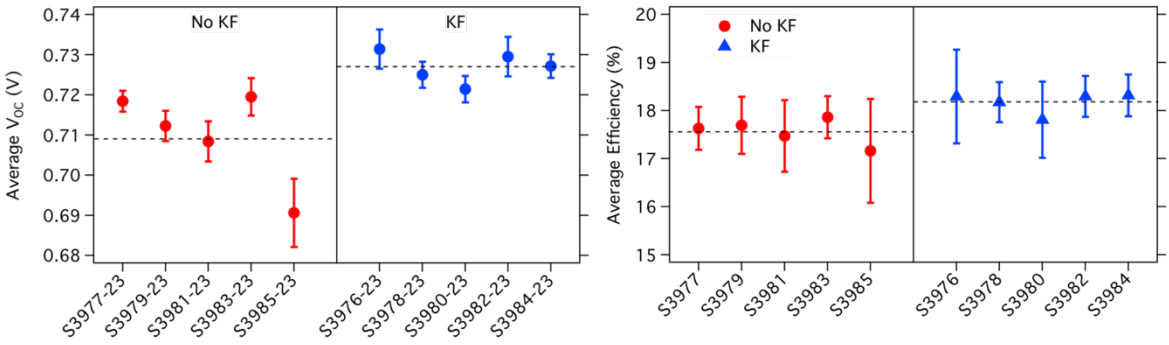

Figure 3. Average V_{OC} versus sample number (left) and average efficiency versus sample (right). Red points are standard runs without KF, and blue points are runs with KF-PDT. Dashed lines show the average overall for each type.

4.1.3. Perform KF PDT on industrial partner samples (AMS 1.1.4)

Alkali post-deposition treatments were performed on samples from two industrial partners. We started with the PDT recipe that gave the best results on NREL CIGS samples: Lamp temp 370°C, KF time 6.5 minutes, and Se rate 35 Å/s. The steps of the experiment were (1) place CIGS absorbers into the deposition chamber with the shutter covering them. (2) Ramp up sample temperature, KF rate, and Se rate. (3) When temperature and rates are reached, open the shutter. (4) Deposit for the allotted time (here 6.5 minutes). (5) Turn down KF, Se, and ramp down temperature. (6) Allow pieces to cool before removing them from the chamber. (7) Rinse pieces in NH_4OH + deionized water. (8) process devices as usual. (9) Perform current-voltage measurements. Samples taken from the same absorber batch, but not given the KF PDT, were fabricated into devices and used as “No KF” controls.

The results for Company A samples are shown in Figure 4. Company A sent the material stack up through CIGS, without CdS and without top contacts. We fabricated the CIGS samples into devices without further processing (No KF, red circles) and with the KF PDT (KF, blue triangles). The devices with KF showed a significant increase in V_{OC} (Figure 4a), accompanied by increases in efficiency (Figure 4b). The best KF devices had V_{OC} increases of over 130 mV and efficiency increases over 5% absolute. The KF PDT was very successful on Company A material, since even the lower-performing samples had average V_{OC} increases of over 50 mV and efficiency increases over 1% absolute.

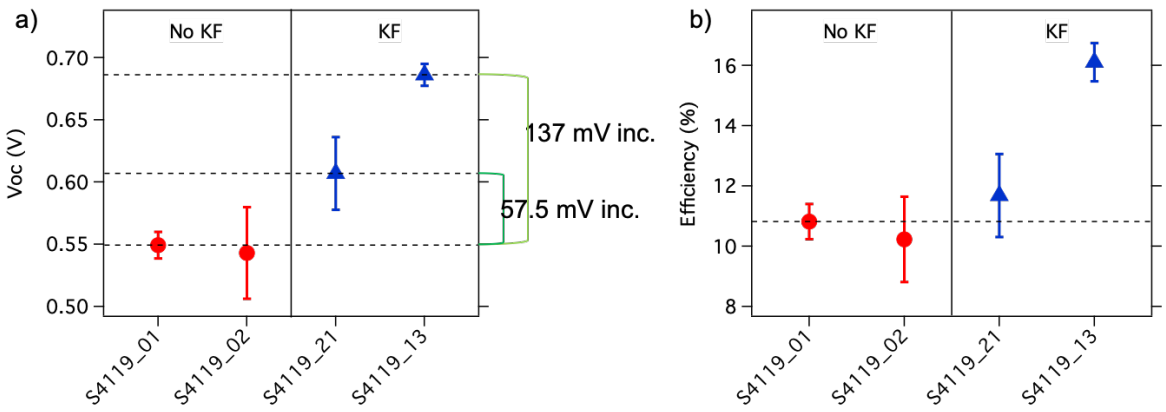

Figure 4. Company A results for a) V_{OC}, and b) efficiency. Red circles indicate devices with no KF and blue triangles have KF PDT.

Company B results are shown in Figure 5. Company B sent the entire device stack. That required the samples to be etched (to remove CdS and transparent conductors) before performing the KF PDT. As with the Company A samples, the best KF samples (Set 2) had a significant increase in V_{OC} (> 45 mV) over the samples with No KF (Figure 5a). The V_{OC} increase came an efficiency increase of greater than 1% absolute (Figure 5b). Sample Set 1 had less impressive results, with the KF PDT increasing the average V_{OC} by 11 mV and introducing variability that can be seen by the large error bars.

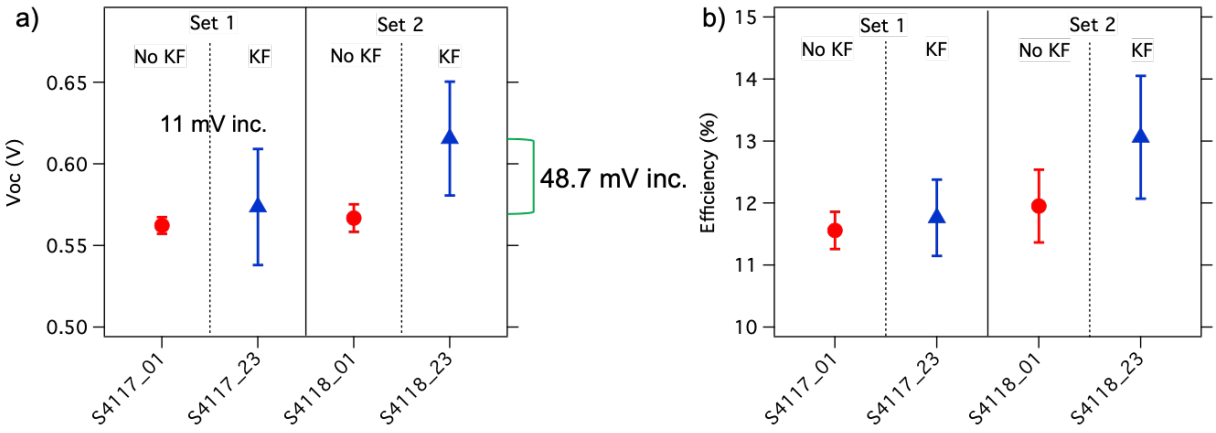

Figure 5. Company B results for a) V_{OC}, and b) efficiency. Red circles indicate devices with no KF and blue triangles have KF PDT.

In the experiments above, some variability in V_{OC} and efficiency was noticed across the samples. If we assume that the material sent by the companies was uniform, which may or may not be the case, then the KF PDT was introducing some non-uniformity. This could be due to a variation in the KF or the Se across the deposition area. The KF source was moved inside the chamber to increase KF uniformity across the samples. We had extra Company B material, so we did extra testing that consisted of applying the KF PDT to 6 samples and fabricating

all of them into devices in the same way. Time-resolved photoluminescence lifetimes and photoluminescence images both improved dramatically after the KF PDT (not shown). Interestingly, these uniformity tests had much higher efficiency values than the original tests, with many devices in Set 2 having efficiency greater than 17%. Company B was pleased with the results and even commented that they never had such good numbers on re-processed (by etching back the top layers and reapplying them) samples.

4.1.4. Incorporate KF into CIGS absorber during deposition (QPI 2.1.1)

To accomplish QPI 2.1.1, KF was introduced at various stages throughout the 3-stage absorber growth. Two baselines were used: a recent absorber without intentional KF introduction ("base") and a film with a particularly successful KF post-deposition treatment. Thirty nm of KF was then co-evaporated along with Cu at the end of the 2nd stage ("End of 2nd") and separately with In/Ga at the end of the 3rd stage ("End of 3rd"). The recipes were repeated to ensure reproducibility. Standard solar cells were fabricated and characterized with current density-voltage (JV), capacitance-voltage (CV), quantum efficiency (QE) as well as secondary ion mass spectrometry (SIMS; with K and Na concentrations calibrated to reference standards). The K distributions that resulted from each recipe are in Figure 6. The KF PDT increased the absorber's mean K content from 0.5×10^{19} cm^{-3} to 3.3×10^{19} cm^{-3}. The "End of 3rd" recipe also reached a high K concentration (5.1×10^{19} cm^{-3}), whereas the "End of 2nd" recipe only had 1.5×10^{19} cm^{-3}. The longer duration at high temperature after evaporating KF in the 2nd stage likely led to K loss by re-evaporation [19], which lowered that sample's final K content.

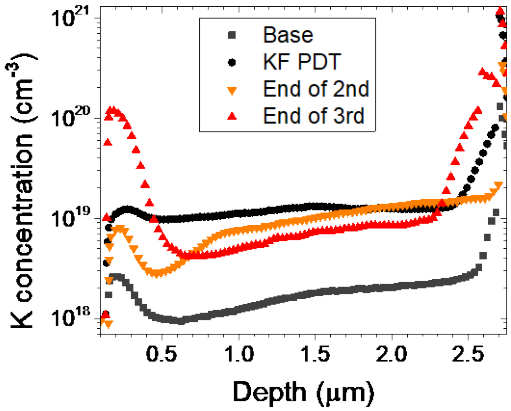

Figure 6. K concentration from SIMS throughout the absorber layer for each recipe.

The photovoltaic (PV) performance for each recipe was evaluated. The KF PDT and "End of 3rd" recipes both resulted in substantial open-circuit voltage and fill factor (V_{OC}/FF) increases, whereas the "End of 2nd" recipe did not. The short-circuit current density (J_{SC}) changes were related to unintentional Ga/(Ga+In) composition and band gap shifts. Band gaps were extracted from QE data for each sample, and the difference between E_g and V_{OC} was used as a levelized voltage comparison. These data (Figure 7) revealed that, relative to the base,

the KF PDT, End of 2nd, and End of 3rd recipes boosted V_{OC} by 25 mV, 6 mV and 21 mV, respectively. The End of 3rd recipe therefore achieved the milestone by reaching a > 20 mV voltage boost and a higher K concentration than the KF PDT.

After reaching the milestone, further work was carried out to understand why the End of 3rd recipe was so much more successful than the End of 2nd. First, the Ga/(Ga+In) profiles from SIMS showed that the End of 2nd recipe had a significantly shallower notch than all of the other samples (Figure 7), despite having similar overall Ga/(Ga+In) composition. This observation suggests that indium out-diffusion from the rear of the absorber, which establishes the Ga/(Ga+In) profile [20], was hindered. It is speculated that In/Ga co-evaporation onto the K-rich surface at the beginning of the 3rd stage formed $KInSe_2$, which reduced indium diffusion and established the undesirable band gap gradient. Since this $KInSe_2$ then experienced a long duration at high temperature without additional K flux, it decomposed and some K was lost by re-evaporation [1]. This result highlights the importance of understanding the heavy alkali metals' chemical reactions and products, which lead to behavior that is different from Na.

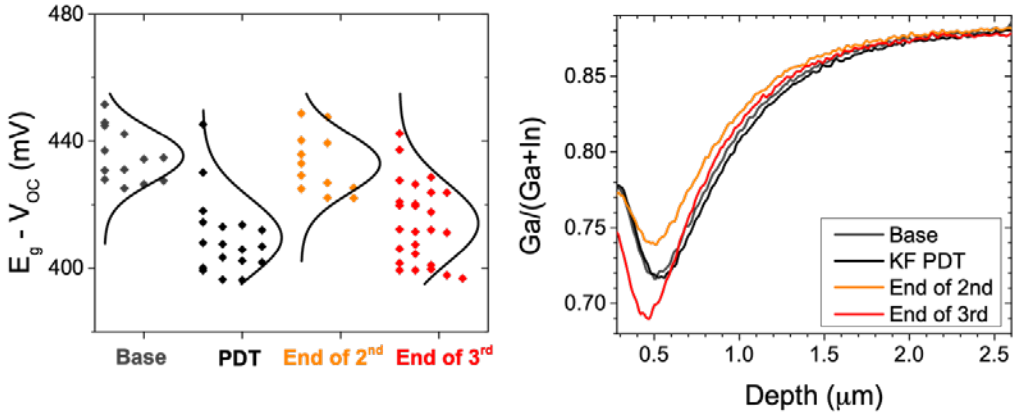

Figure 7. Band gap minus open-circuit voltage (E_g – V_{OC}) for each recipe (left). Ga/(Ga+In) composition from SIMS for each recipe (right).

Next, the Na profiles from SIMS and majority carrier concentrations from CV were examined. The KF PDT caused a reproducible decrease in Na content. This is a well-known effect that occurs when intragranular Na is exchanged for intragranular K at low temperature (350 °C), where the Na is eventually rinsed away during chemical bath deposition of CdS [7]. In contrast, the KF was introduced at higher temperatures (600 °C) for the End of 2nd and End of 3rd recipes. High temperatures do not lead to the intragranular exchange between Na and K, so they had similar mean Na concentrations to the baseline. This interpretation also explains the CV data: all of the devices had similar hole concentrations because they were either doped with Na or K, where both can reduce compensation (e.g., by replacing In_{Cu} with Na_{Cu} or K_{Cu}). The End of 3rd recipe had a high K concentration at its CIGS surface and was cooled directly

after KF evaporation (unlike the End of 2nd recipe). These data indicate that $KInSe_2$ may exist at that sample's CIGS/CdS interface, although its instability in air would make it extremely difficult to directly observe [21]. Finally, the End of 3rd recipe had unchanged carrier concentration and higher voltage, so its performance boost was due to passivation, where surface passivation by $KInSe_2$ is a likely mechanism. In summary, the introduction of KF during CIGS deposition can be successful, although its effects are complex, and chemical reactions/products must be traced more carefully than has historically been done with Na.

4.1.5. Paper on XPS investigation of CIGS with KF PDT (QPI 2.1.2)

In this study, we utilize air-free transfer methods to characterize the effects of KF PDTs. We studied three baseline and three KF PDT samples to improve the statistical robustness of the results. Our KF PDTs boosted efficiency by 6.1% absolute. The data suggest that this improvement is dominated by a reduction in recombination and surface valence band, but the valence-band reduction occurs in the absence of changes to surface Cu or K composition. To explain this and other confounding literature results, we propose that KF, RbF and CsF PDTs reconstruct CIGS surfaces, forming weakly bound Cu-free planes that persist in reducing the valence band even after K, Rb and Cs are rinsed away.

Since the KF PDT advanced efficiency, but not through doping or bulk passivation, we characterized the CIGS surfaces with XPS. We performed XPS before the absorbers are exposed to air, after they are exposed to air, and after an NH_3 rinse. Figure 8(a) shows that the vacuum transfer process leads to negligible oxidation of the surfaces and that the NH_3 rinse successfully removes the oxides that form after air exposure. Figure 8(b) shows that the as deposited and air exposed KF PDT samples have fluoride compounds that must be rinsed away (along with the oxides) for band energy data to be attributable to the device-relevant semiconductors. Figure 8(c) shows that the NH_3 rinse also tends to reduce K to below the detection limit for XPS, although SIMS on devices shows that 0.1 – 0.3% (vol/vol) K is retained at the CIGS/CdS interface. Figure 8(d) shows that the baseline samples had Na on their surfaces, and the KF PDT samples increased that Na.

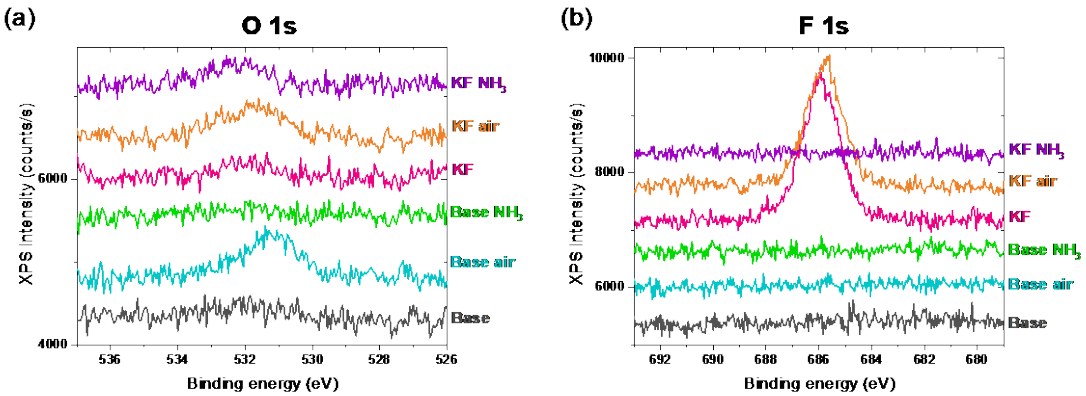

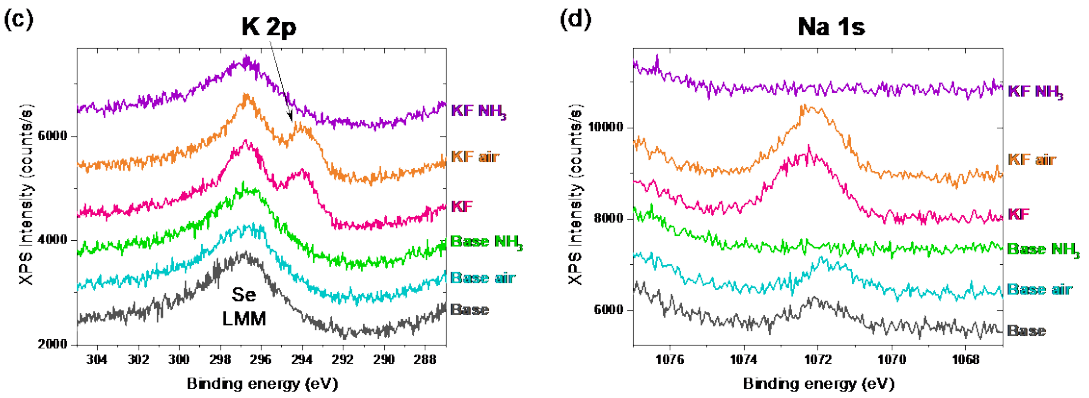

Figure 8. XPS detailed spectra of the (a) O 1s, (b) F 1s, (c) K 2p, and (d) Na 1s peaks for the as deposited (gray), air exposed (light blue), and NH_3 rinsed (green) Base-2 sample, as well as the as deposited (pink), air exposed (orange), and NH_3 rinsed (purple) KF-2 sample.

We examined the NH_3 rinsed XPS data in more detail in Figure 9 and found that Base-1 had slightly less Cu and KF-2 had significantly less Cu, but otherwise the samples had similar Cu peaks. On the other hand, the KF PDT clearly reduced Ga in Figure 9(b), possibly through the formation of some soluble gallium compound that was rinsed away. The KF-2 sample also shows less In, while all other samples had similar In peaks in Figure 9(c). Quantitative XPS compositions of the NH_3 rinsed samples showed that the KF PDT is associated with increased K, Cu, In and Se, as well as decreased Ga. We also corrected sensitivity factors and inelastic mean free paths to depend on composition, which slightly changes the results. The correction increased Cu while decreasing In and Ga, while also increasing Cu's standard deviation. Overall, we conclude that the PDT reduced Ga and did not significantly change Cu or K.

Hence, XPS does not show a significant decrease in Cu/(Ga+In) or increase in K/(K+Cu). We propose that instead, KF PDTs reduce the valence band by reconstructing the surface from chalcopyrite CIGS to layered $K_2CuIn_3Se_6$ or $KInSe_2$. The formation of this 3D/2D structure passivates and forms Cu-free cation planes that may reduce valence band even after K is rinsed away. The full paper containing more details about the surface reconstruction will be submitted to ACS Applied Energy Materials [22].

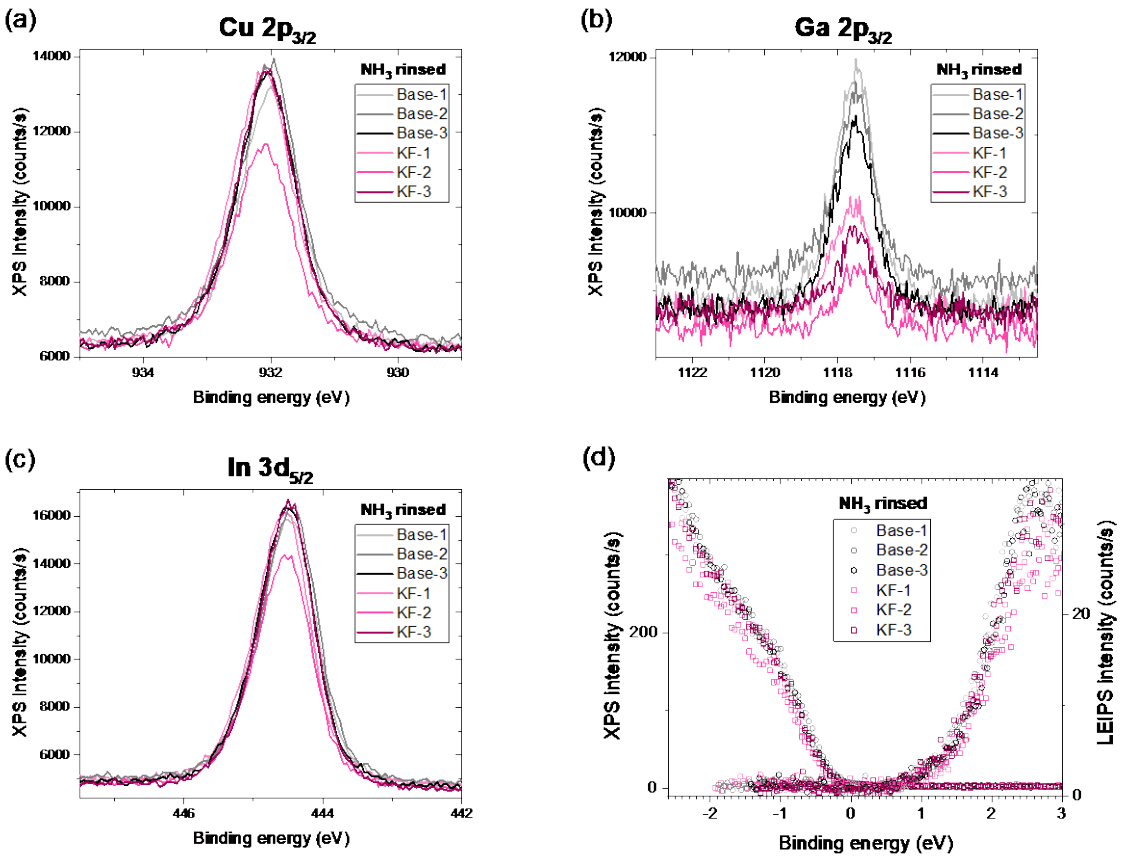

Figure 9. XPS detailed spectra of the (a) Cu 2p3/2, (b) Ga 2p3/2, (c) In 3d5/2 peaks, and (d) XPS valence band energy relative to Fermi energy ($E_F - E_{VB}$; left axis) and LEIPS conduction band energy relative to Fermi energy ($E_{CB} - E_F$; right axis) for the NH_3 rinsed Base-1 (light gray circles), Base-2 (gray circles), Base-3 (black circles), KF-1 (light pink squares), KF-2 (pink squares), and KF-3 (dark pink squares) samples.

4.1.6. Increase V_{OC} by 20 mV with RbF PDT (QPI 2.1.3)

After significant investigation, we were able to increase V_{OC} and efficiency in devices by applying an RbF PDT. The bandgap minus V_{OC} results are shown in Figure 10. The data are split by side of the sample because our system has a small gradient which produces lower Ga on the -11 side and higher Ga on the -23 side. A difference of 24 mV to 30 mV between RbF PDT and standard (no RbF) samples was achieved.

The recipe for the best RbF PDT occurs when the RbF cell temperature is 540°C and the lamp setpoint temperature (T_{lamps}) is 460°C. The RbF cell temperature (T_{RbF}) was held at a warming temperature of 400°C during the CIGS deposition. At the end of the 3rd stage of CIGS deposition, T_{RbF} was ramped up at 30°C/min to 450°C. After the 3rd stage, the substrate temperature was ramped down (21.5°C/min). When it reached 460°C the temperature ramp was interrupted and held there for 9 minutes during the RbF PDT. In this deposition system, the actual substrate temperature is approximately 10°C lower than T_{lamps} in the RbF-PDT temperature range. The Se rate was adjusted to be 25 Å/s for the 9-minute PDT duration and during any subsequent substrate temperature cool down to a

lamp temperature of 300°C. At the end of the 4-minute RbF deposition time, the RbF cell was quenched by cutting its power. More information can be found in the upcoming publication [23].

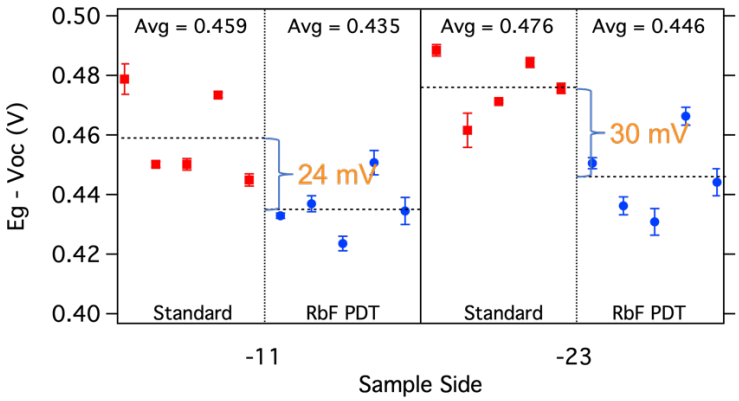

Figure 10. E_g-V_{OC} for standard runs (no PDT, red squares) and RbF PDT runs (blue circles). The data is broken up by sample side.

4.1.7. Unmet QPIs and AMS

Two QPIs (3.1.1, 3.1.2) and one AMS (3.1.4) went unmet for Task 1. QPI 3.1.2 was to submit paper on XPS investigation of CIGS with RbF. Because of XPS downtime and installing a new instrument, we did not get to working with RbF samples in the XPS. Instead, we submitted a paper on setting boundaries on the recipe for the RbF PDT. QPI 3.1.1 was to demonstrate 30 mV V_{OC} and/or 1.5% efficiency improvement in the samples from at least one industrial partner. AMS 3.1.4 was to submit a paper on alkali mechanisms and outlook for manufacturability, plus demonstrate at least 2% absolute device efficiency improvement on an industrial partner's absorber using alkalis. We did not meet these because of the lack of industrial partners. Details of the difficulties encountered are given in section 19.

4.2. Task 2: Cell-level Reliability

4.2.1. Sentaurus model predicting reverse-bias behavior (QPI 1.2.3)

In our previous project we showed that reverse bias characteristics of CIGS devices could be controlled by changing the buffer and window layers. In particular, removing the iZnO layer from CIGS devices allowed them to flow current density of J_{mpp} in reverse without damage. We continued to investigate this phenomenon through Sentaurus device modeling for QPI 1.2.3. We modeled different device stacks both with and without the iZnO layer. Then we simulated electric field, band bending, and current-density voltage (J-V) curves in reverse bias. Figure 11 (top) shows the electric field near the front of the devices. By comparing the graphs on the right and left, you can tell that the graph on the right has a higher electric field both in the CdS layer and the CIGS layer. The bottom graphs show the band bending at -1.5 V for each device configuration. Arrows show a possible tunneling path on each graph, which is shorter for the sample without the iZnO layer (right). Both the electric field and

the band bending confirm that tunneling, and hence a higher magnitude of current, are more likely in the devices that do not contain an iZnO layer.

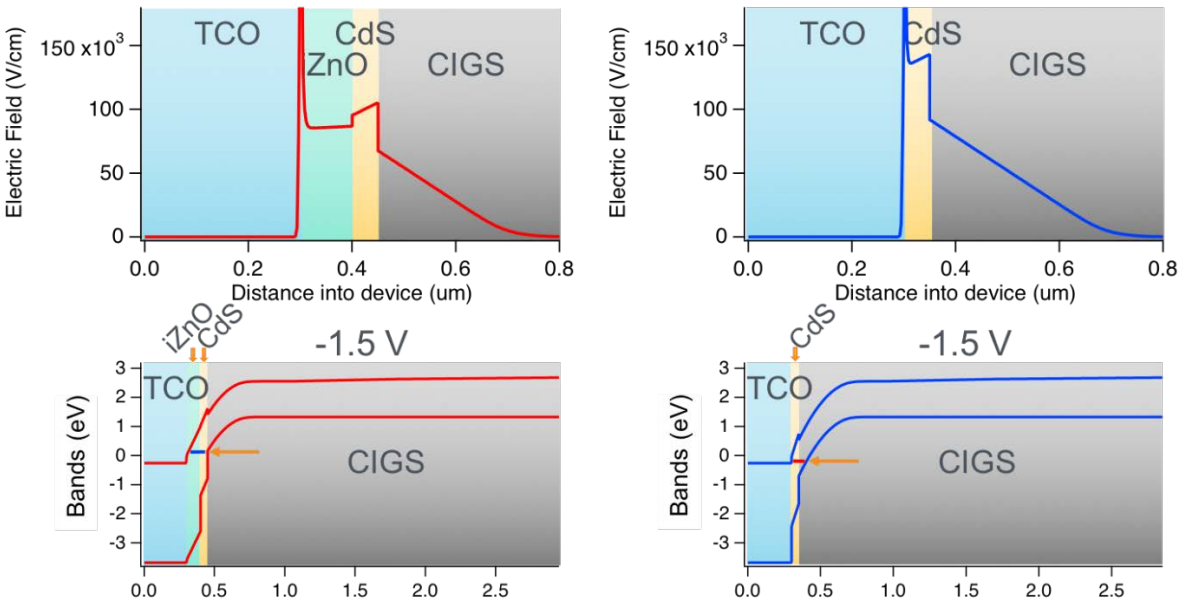

Figure 11. Simulated electric fields at -1 V (top) and bands at -1.5 V (bottom) of devices with iZnO (left) and without iZnO (right). Arrows in bottom graphs show a possible tunneling path that is shorter for the sample without iZnO (right).

Figure 12 shows simulated reverse-bias J-V curves for the samples with iZnO and without iZnO. The top curve (red dashed) is the iZnO simulation. Even without accounting for tunneling, the curve for no iZnO (blue dashed) has a higher magnitude of current density at the same reverse voltages. After adding tunneling to the simulation, the magnitude of current density increases for the device with iZnO (red solid) as expected. The simulation for the device without iZnO, with tunneling added (blue solid) shows an even greater increase in magnitude of current density. One thing to note, these curves do not match our measured devices. In particular, they flatten out at larger magnitudes of reverse-bias voltage, whereas at some point the current density of measured devices increases exponentially. This difference could occur for a few different reasons, such as the possibility of one or more of several different tunneling mechanisms being responsible for the measured device behavior. Other possibilities include the devices being slightly damaged by the high reverse current, and then recovering. This would be much more difficult to simulate with a device model. To complete QPI 1.2.3, we needed to show that, “the experimental trends of the Zn(O,S) device flowing more current at lower reverse voltages than the CdS device should be apparent.” This is confirmed with Figure 12.

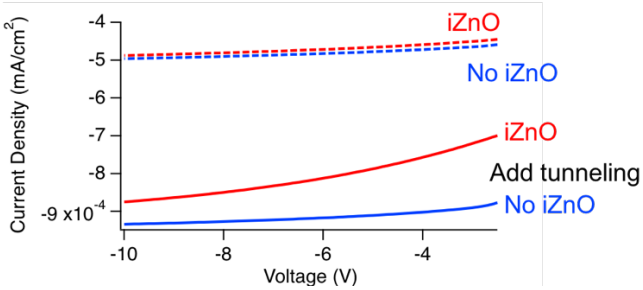

Figure 12.Simulated reverse-bias curves for devices with (red) and without (blue) iZnO. Simulations without tunneling (dashed) and with tunneling (solid) are shown. Devices without iZnO consistently flow a higher magnitude of current density at the same reverse-bias voltages.

4.2.2. Decreased metastability with hole-injection layer

Because metastability is dependent on buffer layer properties [24], we were curious about what buffer modifications could increase device stability. We found that adding small amounts of CdS to either side of the Zn(O,S) (Figure 13 left) reduced the amount of metastability when compared to devices with Zn(O,S) alone (Figure 13 right). When comparable amounts of CdS are included, it is more effective to inject holes from the front (light) side of the Zn(O,S) than from the CIGS side of the Zn(O,S). This distinction implies that the presence of holes in the buffer or the buffer/ZnO interface, not just in a defective layer at the CIGS surface, is important to metastability. There is little to no voltage penalty for the use of the Zn(O,S) buffer in conjunction with thin CdS, particularly when the thin CdS is added on top of the Zn(O,S). The use of very thin CdS allows the benefit of high currents (like devices with Zn(O, S)-only buffers) simultaneously with high voltage (like devices CdS-only buffers). The most effective buffer variant in this study produces devices without metastability and with higher efficiency than the CdS-only controls (Figure 13 right). When the CdS is added on top of the Zn(O,S), it can only change interface recombination at the CIGS surface by moving the Fermi level away from mid-gap, not by defect passivation. The increased performance and decreased metastability via hole injection is not expected to be unique to CdS. Any material that can be used to inject holes is expected to work in a similar manner. The full discussion of this experiment can be found in reference [25].

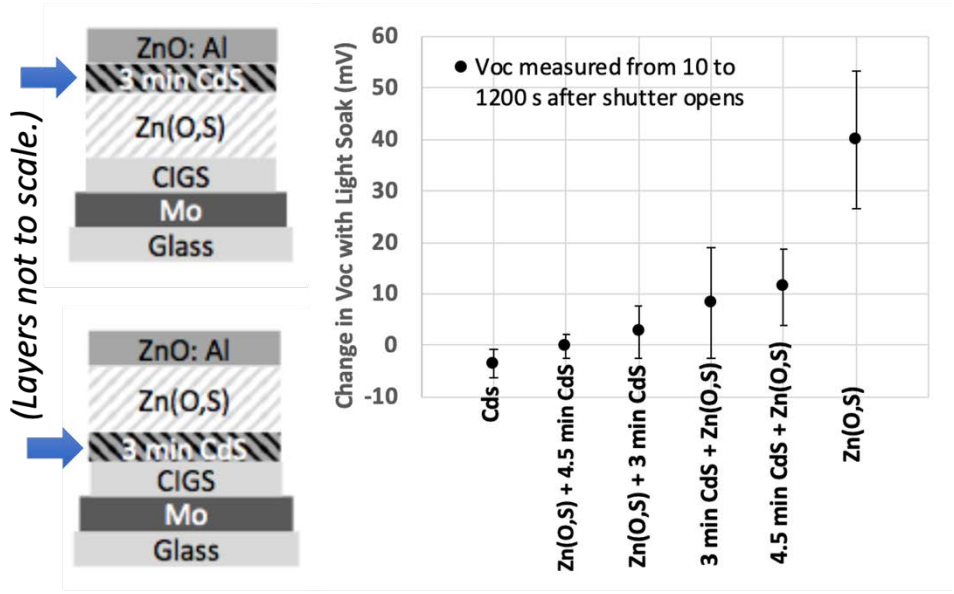

Figure 13. Schematic of buffer structures (left). Layers are not to scale. Change in V_{OC} as a function of buffer structure (right).

4.2.3. Increased time to PID by 2X (AMS 2.2.4)

Potential-induced degradation can occur from voltage across the back glass or across the front glass. In the FY16-FY19 project, we studied back-glass PID because it happens much quicker and so is more well-known. For this project, we studied front-glass PID. We compared samples with two different types of glass 1) Na-rich soda-lime glass (SLG) and 2) K-rich borosilicate glass (BSG). Samples were biased with 1000 V applied to an aluminum tape on the front side of the glass and the cells grounded (Figure 14 left). Performance degradation was normalized by dividing by the initial efficiency (η/η_0) and then dividing the high voltage stress sample (85 °C; +1000 V) by the control sample (85 °C). Results over 1600 hours of stressing is shown in Figure 14(right). Final normalized efficiency for SLG was 0.44, whereas for BSG it was 1.07, proving that time to PID could be increased by using borosilicate front glass.

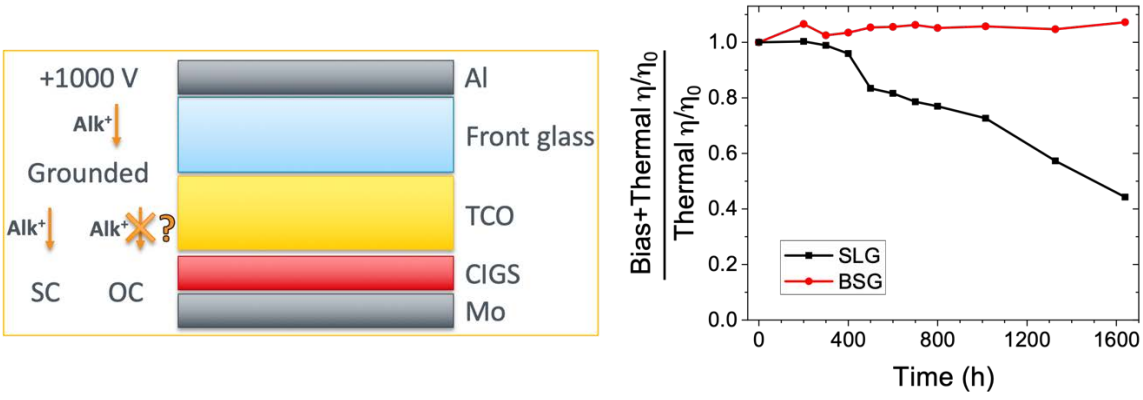

Figure 14. Schematic of a CIGS sample with front-glass bias (left), and graph of normalized efficiency versus stress time (right).

4.2.4. Additional PID discoveries

As we further studied PID, discrepancies led us to additional questions. We found that the reduction in efficiency associated with damage did not perfectly correlate to the charge transferred across the glass for different substrate types (and thus conductivities). This became apparent when we PID stressed devices on soda-lime glass with an Al_2O_3 alkali diffusion barrier. The Al_2O_3 diffusion barrier had little effect on leakage current, but still slowed the time to PID failure by 5x, relative to baseline SLG. Moreover, SLG, Al_2O_3 and BSG samples all had different PID vs. Coulombs transferred slopes. A simple alkali-metal-cation mass-balance model may explain this unexpected result: when stress was interrupted to characterize devices with light/electrical bias, PID was partially reversed. Additional experiments showed that holding devices at open-circuit conditions during high voltage stress achieved a similar effect. Therefore, illumination and device bias are both ways to drive alkali metal cations away from the p-n junction, perhaps reducing test-specific degradation.

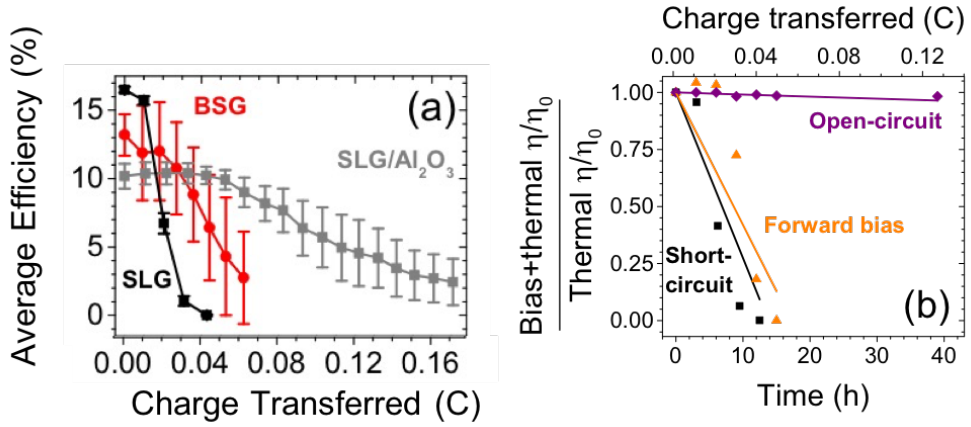

Figure 15. Mean efficiency (a) with standard deviation (error bars) as a function of cumulative charge transferred through leakage current at -1000 V bias, 85 °C and 10% RH for SLG (black squares), SLG/Al_2O_3 (gray squares), and BSG (red circles) substrates. Mean efficiency normalized (b) to initial mean efficiency at -1000 V bias, 85 °C and 10% RH, then divided by mean efficiency normalized to initial mean efficiency at 85 °C and 10% RH (control) as a function of time (bottom) and cumulative charge transferred through leakage current (top) for SLG samples at short-circuit (standard baseline; black squares), forward bias (orange triangles), and open-circuit (purple diamonds). Lines are calculated from the model for short-circuit (black), forward bias (orange), and open-circuit (purple) conditions.

The results are summarized in Table 3. It shows a summary of light and electrical bias conditions, their PID effects, and example mechanisms for how illuminated and dark open-circuit conditions may help avoid test-specific degradation. The arrows indicate transport toward the Mo or CdS side, where Alk^+ in the p-n junction is assumed to be more harmful. They are significant because they indicate that the standard IEC testing configuration for PID, which is specified for crystalline silicon modules to be dark and short-circuit, may lead to test-specific degradation. A more field-relevant test may be performed in the laboratory by illuminating during PID stress: an option that is specified in IEC TS 62804-2, the technical specification for the PID testing of thin-film modules that

is being drafted. Alternatively, dark open-circuit or reverse-bias conditions are candidates for consideration, but further work would be necessary to correlate such test states with field PID. The electrical bias techniques may be simple, low-cost alternatives to illuminating modules during high-voltage stress. In particular, quantifying atomic mobilities of alkali metal cations through various media and under various conditions would be valuable for testing the mechanisms proposed in Table 3. These results show that light/electrical bias of CIGS devices should be carefully controlled when testing PID [26].

Table 3. Summary of light and electrical bias conditions and their PID effects.

Light	Electrical	PID effect	Mechanism
Dark	Short-circuit	Degrading	Alk^+ diffuse → CdS Mo ← e^- drift
	Forward bias	Degrading	Mo ← e^- drift Alk^+ drift → CdS
	Open-circuit	Benign	No net e^- transport No net Alk^+ transport
Light	Any	Benign	e^- drift → CdS Mo ← Alk^+ drift

In an additional paper [27], two types of CIGS PID are characterized. The first, front shunting PID, is driven by front-glass stress and occurs when alkali metal cations accumulate in the i-ZnO buffer, where they increase shunt conductance to reduce fill factor. The second, p-n junction PID, results from back-glass stress as alkali metal cations pile up near the CIGS surface/CdS buffer, where they reduce charge carrier concentration, open-circuit voltage, and fill factor to degrade efficiency ~160 times faster than front shunting PID. These results illuminate how PID occurs in CIGS, how to reduce it, and how to test for it.

4.2.5. Report on testing and measuring cell-level reliability (QPI 3.2.3)

For the final QPI on cell-level reliability, we documented testing procedures and discussed challenges for measuring reliability at the cell level in reference [17]. We were able to reproduce issues that occur at the module level in small-area CIGS cells. Measurement protocols were developed for metastability, shading-induced damage, and potential-induced degradation. The procedures can be applied to laboratory-scale devices of other photovoltaic technologies as well. The techniques allow researchers to investigate reliability earlier in the research cycle, which can potentially avoid common reliability problems. This can save time, reduce scale-up costs, and prevent damage to the public's perception of newer PV technologies.

5. Significant Accomplishments and Conclusions

Significant accomplishments of this program are listed below.

- KF post-deposition treatments were shown to improve lifetime, V_{OC}, and efficiency of industrial partner samples, even when done as a later step, separate from the original CIGS deposition.
- KF boosted efficiency when incorporated at the end of the third stage of NREL CIGS growth.
- XPS characterization of CIGS surfaces with and without PDTs shows that rinsing the samples with NH_3 removes some oxides formed during air exposure, and also removes excess surface Na and K. This led to a proposed mechanism whereby K drives structural transformation at 350 °C that is locked in at room temperature even after K is rinsed away.
- Published recipes for KF and RbF PDTs. Literature to date did not provide enough detail to quickly reproduce experimental results.
- Identified most important parameters (RbF cell temperature and lamp setpoint temperature) and set boundaries for successful RbF PDTs.
- Published NREL's cell-level reliability testing procedures along with challenges that were encountered while developing them. These were also distributed to the community through an MRS conference presentation.
- Decreased metastability by adding a CdS hole-injection layer between the CIGS and Zn(O,S) in the device stack. It also improved device performance. Materials other than CdS can be used for the same purpose.
- Reduced front-glass PID by replacing soda-lime glass with low-Na borosilicate glass.
- Found that PID depends on leakage current and light/electrical bias. This will help labs avoid test-specific degradation.
- Discovered that CIGS can suffer from two different types of PID. Front is slower and leads to shunting ZnO. Back is faster and degrades the p-n junction.
- Holding cells at open circuit slows PID compared to short circuit. This affects testing protocols for glass/glass modules.

A few challenges were encountered under this award.

- The XPS studies that we had planned relied on a system that experienced significant downtime. It was finally retired and a new XPS instrument was installed in time to complete only one XPS study.
- It was difficult to maintain high baseline CIGS device efficiencies using the MBE tool, which was needed to complete air-free transfers for XPS studies.
- The most significant challenge was that the CIGS industry contracted dramatically during the three years of the project. In FY19 Q2, four CIGS companies had signed agreements with NREL to share samples. Nine months later, one was closed, and two foreign-purchased companies were 'temporarily' halting production. By the end of 2020, all three were closed, and the last existing company with production capacity was not responding. This

caused one QPI (3.1.1) and one milestone (3.1.4) to go unmet because they relied on industrial partner samples, collaboration, and feedback.

6. Budget and Schedule

Cumulative spending through project end month was $2,910,446.33. Figure 16 shows the information from the RPPR-2 form. The initial period of performance was 12 quarters. A two-quarter no-cost extension was granted to allow completion of publications and reports. There will be expenditures for finishing papers, creating the final presentation, and writing the final report during the 90-day close-out period following the end of the project.

Project Spend Plan			Federal Share			Recipient Share		
Quarter	From	To	Initial Plan	Actuals & Updated Plan	Cumulative	Initial Plan	Actuals & Updated Plan	Cumulative
1	10/01/18	12/31/18	$ 241,374.25	$ 171,201.01	$171,201.01			$0.00
2	01/01/19	03/31/19	$ 241,374.25	$ 222,484.96	$393,685.97			$0.00
3	04/01/19	06/30/19	$ 241,374.25	$ 307,893.56	$701,579.53			$0.00
4	07/01/19	09/30/19	$ 241,374.25	$ 313,241.90	$1,014,821.43			$0.00
5	10/01/19	12/31/19	$ 249,070.25	$ 190,231.72	$1,205,053.15			$0.00
6	01/01/20	03/31/20	$ 249,070.25	$ 196,962.40	$1,402,015.55			$0.00
7	04/01/20	06/30/20	$ 249,070.25	$ 184,664.48	$1,586,680.03			$0.00
8	07/01/20	09/30/20	$ 249,070.25	$ 199,415.97	$1,786,096.00			$0.00
9	10/01/20	12/31/20	$ 171,609.00	$ 175,297.13	$1,961,393.13			$0.00
10	01/01/21	03/31/21	$ 171,609.00	$ 270,989.18	$2,232,382.31			$0.00
11	04/01/21	06/30/21	$ 171,609.00	$ 255,880.35	$2,488,262.66			$0.00
12	07/01/21	09/30/21	$ 171,609.00	$ 187,086.07	$2,675,348.73			$0.00
13	10/01/21	12/31/21	$ 171,609.00	$ 138,953.09	$2,814,301.82			$0.00
14	01/01/22	03/31/22	$ 171,609.00	$ 96,144.51	$2,910,446.33			$0.00
15	04/01/22	06/30/22		$80,985.67	$2,991,432.00			$0.00
16	07/01/22	09/30/22			$2,991,432.00			$0.00
Totals			$2,991,432.00	$2,991,432.00	$2,991,432.00	$0.00	$0.00	$0.00
			Updated Federal Spend Plan			Updated Recipient Spend Plan		

Figure 16. Picture from the RPPR-2 showing the spending plan and actual expenditures.

7. Path Forward

Due to the lack of industrial activity in this area, the future of CIGS research and development at NREL looks bleak. CIGS remains a great solar technology that is stable and reliable. It can make excellent bottom cells for tandem technologies, and is especially useful for lightweight and flexible applications. This may enable a resurgence of CIGS technology in the future. Breakthroughs in processing at scale could also reduce capital expenditures, allowing higher profit margins than are possible today.

8. Inventions, Patents, Publications, and Other Results

8.1. Peer-Reviewed Journal Articles

1. M.C. Alonso-Garcia, P. Hacke, S. Glynn, C.P. Muzzillo, L.M. Mansfield, Analysis of Potential-Induced Degradation in Soda-Lime Glass and Borosilicate-Glass Cu(In,Ga)Se_2 Samples, IEEE J. Photovolt. 9 (2019) 331–338. https://doi.org/10.1109/JPHOTOV.2018.2882195.

2. J. Bailey, D. Poplavskyy, G. Zapalac, L. Mansfield, W. Shafarman, Voltage-Induced Charge Redistribution in Cu(In,Ga)Se_2 Devices Studied With High-Speed Capacitance–Voltage Profiling, IEEE J. Photovolt. 9 (2019) 319–324. https://doi.org/10.1109/JPHOTOV.2018.2882204.
3. S.P. Harvey, H. Guthrey, C.P. Muzzillo, G. Teeter, L. Mansfield, P. Hacke, S. Johnston, M. Al-Jassim, Investigating PID Shunting in Polycrystalline CIGS Devices via Multi-Scale, Multi-Technique Characterization, IEEE J. Photovolt. 9 (2019) 559–564. https://doi.org/10.1109/JPHOTOV.2019.2892874.
4. C.-S. Jiang, L.M. Mansfield, S. Glynn, C. Xiao, R. Garris, S. Christensen, M. Al-Jassim, Effect of Window-Layer Materials on p-n Junction Location in Cu(In,Ga)Se_2 Solar Cells, IEEE J. Photovolt. 9 (2019) 308–312. https://doi.org/10.1109/JPHOTOV.2018.2874039.
5. D.H. Kim, C.P. Muzzillo, J. Tong, A.F. Palmstrom, B.W. Larson, C. Choi, S.P. Harvey, S. Glynn, J.B. Whitaker, F. Zhang, Z. Li, H. Lu, M.F.A.M. van Hest, J.J. Berry, L.M. Mansfield, Y. Huang, Y. Yan, K. Zhu, Bimolecular Additives Improve Wide-Band-Gap Perovskites for Efficient Tandem Solar Cells with CIGS, Joule. 3 (2019) 1734–1745. https://doi.org/10.1016/j.joule.2019.04.012.
6. L.M. Mansfield, S. Glynn, S. Johnston, C. Marshall, C.P. Muzzillo, B. Stevens, M.R. Young, Setting boundaries on the recipe for a successful RbF post-deposition treatment of CIGS, Submitt. Sol. Energy Mater. Sol. Cells. (n.d.).
7. L.M. Mansfield, C.P. Muzzillo, S. Glynn, I.L. Repins, Cell-level reliability testing procedures for CIGS photovoltaics, MRS Adv. 6 (2021) 599–608. https://doi.org/10.1557/s43580-021-00107-z.
8. D.L. McGott, C.P. Muzzillo, C.L. Perkins, J.J. Berry, K. Zhu, J.N. Duenow, E. Colegrove, C.A. Wolden, M.O. Reese, 3D/2D passivation as a secret to success for polycrystalline thin-film solar cells, Joule. 5 (2021) 1057–1073. https://doi.org/10.1016/j.joule.2021.03.015.
9. M. Mezher, L.M. Mansfield, K. Horsley, W. Yang, M. Blum, L. Weinhardt, K. Ramanathan, C. Heske, Variations in the Chemical and Electronic Impact of Post-Deposition Treatments on Cu(In,Ga)$(S,Se)_2$ Absorbers, ACS Appl. Energy Mater. 2 (2019) 8641–8648. https://doi.org/10.1021/acsaem.9b01565.
10. C.P. Muzzillo, S. Glynn, P. Hacke, H.R. Moutinho, M.R. Young, I.L. Repins, L.M. Mansfield, Potential-Induced Degradation Depends on Leakage Current and Light/Electrical Bias in Cu(In,Ga)Se_2 Devices, IEEE J. Photovolt. 9 (2019) 1852–1856. https://doi.org/10.1109/JPHOTOV.2019.2933189.
11. C.P. Muzzillo, S. Glynn, G. Teeter, L.M. Mansfield, K, Rb, and Cs improve Cu(In,Ga)Se_2 surface band alignment through reconstruction, (n.d.).
12. C.P. Muzzillo, K. Terwilliger, P. Hacke, H.R. Moutinho, M.R. Young, S. Glynn, B. Stevens, I.L. Repins, L.M. Mansfield, Potential-induced degradation of Cu(In,Ga)Se_2 can occur by shunting the front i-ZnO and by damaging the p-n junction, Sol. Energy. 232 (2022) 298–303. https://doi.org/10.1016/j.solener.2021.12.074.

13. I. Repins, S. Glynn, K. Bowers, B. Stevens, C.L. Perkins, L. Mansfield, Using hole injection layers for decreased metastability and higher performance in Cu(In,Ga)Se_2 devices, Sol. Energy Mater. Sol. Cells. 215 (2020) 110597. https://doi.org/10.1016/j.solmat.2020.110597.
14. I. Repins, S. Glynn, T.J. Silverman, R. Garris, K. Bowers, B. Stevens, L. Mansfield, Large metastability in Cu (In,Ga)Se_2 devices: The importance of buffer properties, Prog. Photovolt. Res. Appl. 27 (2019) 749–759. https://doi.org/10.1002/pip.3145.
15. B.J. Stanbery, D. Abou-Ras, A. Yamada, L. Mansfield, CIGS photovoltaics: reviewing an evolving paradigm, J. Phys. Appl. Phys. 55 (2022) 173001. https://doi.org/10.1088/1361-6463/ac4363.
16. G.M. Wilson, M. Al-Jassim, W.K. Metzger, S.W. Glunz, P. Verlinden, G. Xiong, L.M. Mansfield, B.J. Stanbery, K. Zhu, Y. Yan, J.J. Berry, A.J. Ptak, F. Dimroth, B.M. Kayes, A.C. Tamboli, R. Peibst, K. Catchpole, M.O. Reese, C.S. Klinga, P. Denholm, M. Morjaria, M.G. Deceglie, J.M. Freeman, M.A. Mikofski, D.C. Jordan, G. TamizhMani, D.B. Sulas-Kern, The 2020 photovoltaic technologies roadmap, J. Phys. Appl. Phys. 53 (2020) 493001. https://doi.org/10.1088/1361-6463/ab9c6a.

8.2. Conference Publications

1. L.M. Mansfield, K. Bowers, S. Glynn, I.L. Repins, The Effects of Absorber Thickness on Reverse-Bias Damage in Cu(In,Ga)Se_2 Solar Cells, in: 2019 IEEE 46th Photovolt. Spec. Conf. PVSC, IEEE, Chicago, IL, USA, 2019: pp. 3201–3205. https://doi.org/10.1109/PVSC40753.2019.8981307.
2. C. Xiao, C.-S. Jiang, S.P. Harvey, L. Mansfield, C.P. Muzzillo, D. Sulas, J. Liu, S. Johnston, M. Al-Jassim, In-situ Microscopy Characterization of Cu(In,Ga)Se_2 Potential-Induced Degradation, in: 2019 IEEE 46th Photovolt. Spec. Conf. PVSC, IEEE, Chicago, IL, USA, 2019: pp. 2342–2345. https://doi.org/10.1109/PVSC40753.2019.8980888.

8.3. Conference Presentations

1. S.P. Harvey, Utilizing TOF-SIMS to Investigate Module Degradation Mechanisms, (2019).
2. L.M. Mansfield, The Effects of Absorber Thickness on Reverse-Bias Damage in Cu(In,Ga)Se_2 Solar Cells, (2019).
3. L.M. Mansfield, Cell-Level Reliability Starring CIGS Thin-Film PV, (2021).
4. W.K. Metzger, G. Xiong, L.M. Mansfield, B.J. Stanbery, X. Wu, Chalcogenide PV Roadmap (Panel), (2020).
5. C.P. Muzzillo, Potential-Induced Degradation Depends on Leakage Current and Light/Electrical Bias in Cu(In,Ga)Se_2 Devices, (2019).
6. C. Xiao, In-situ Microscopy Characterization of Cu(In,Ga)Se_2 Potential-Induced Degradation, (2019).

9. References

[1] M. Nakamura, K. Yamaguchi, Y. Kimoto, Y. Yasaki, T. Kato, and H. Sugimoto, "Cd-Free Cu(In,Ga)(Se,S) $_2$ Thin-Film Solar Cell With Record Efficiency of 23.35%," *IEEE J. Photovolt.*, vol. 9, no. 6, pp. 1863–1867, Nov. 2019, doi: 10.1109/JPHOTOV.2019.2937218.

[2] S. Ishizuka, N. Taguchi, and P. J. Fons, "Similarities and Critical Differences in Heavy Alkali-Metal Rubidium and Cesium Effects on Chalcopyrite Cu(In,Ga)Se $_2$ Thin-Film Solar Cells," *J. Phys. Chem. C*, vol. 123, no. 29, pp. 17757–17764, Jul. 2019, doi: 10.1021/acs.jpcc.9b06042.

[3] D. L. McGott *et al.*, "3D/2D passivation as a secret to success for polycrystalline thin-film solar cells," *Joule*, vol. 5, no. 5, pp. 1057–1073, May 2021, doi: 10.1016/j.joule.2021.03.015.

[4] E. Handick *et al.*, "Potassium Postdeposition Treatment-Induced Band Gap Widening at Cu(In,Ga)Se $_2$ Surfaces – Reason for Performance Leap?," *ACS Appl. Mater. Interfaces*, vol. 7, no. 49, pp. 27414–27420, Dec. 2015, doi: 10.1021/acsami.5b09231.

[5] C. P. Muzzillo, J. V. Li, L. M. Mansfield, K. Ramanathan, and T. J. Anderson, "Surface and bulk effects of K in highly efficient Cu1-xKxInSe2 solar cells," *Sol. Energy Mater. Sol. Cells*, vol. 185, pp. 45–53, Oct. 2018, doi: 10.1016/j.solmat.2018.05.013.

[6] C. P. Muzzillo, H. M. Tong, and T. J. Anderson, "The effect of Na on Cu-K-In-Se thin film growth," *J. Cryst. Growth*, vol. 488, pp. 36–42, Apr. 2018, doi: 10.1016/j.jcrysgro.2018.02.035.

[7] C. P. Muzzillo, "Review of grain interior, grain boundary, and interface effects of K in CIGS solar cells: Mechanisms for performance enhancement," *Sol. Energy Mater. Sol. Cells*, vol. 172, pp. 18–24, Dec. 2017, doi: 10.1016/j.solmat.2017.07.006.

[8] Y. Wang, S. Lv, and Z. Li, "Review on incorporation of alkali elements and their effects in Cu(In,Ga)Se2 solar cells," *J. Mater. Sci. Technol.*, vol. 96, pp. 179–189, Jan. 2022, doi: 10.1016/j.jmst.2020.07.050.

[9] S. Siebentritt *et al.*, "Heavy Alkali Treatment of Cu(In,Ga)Se $_2$ Solar Cells: Surface versus Bulk Effects," *Adv. Energy Mater.*, vol. 10, no. 8, p. 1903752, Feb. 2020, doi: 10.1002/aenm.201903752.

[10] Y. Sun *et al.*, "Review on Alkali Element Doping in Cu(In,Ga)Se 2 Thin Films and Solar Cells," *Engineering*, vol. 3, no. 4, pp. 452–459, Aug. 2017, doi: 10.1016/J.ENG.2017.04.020.

[11] I. Khatri, T. Yashiro, T.-Y. Lin, M. Sugiyama, and T. Nakada, "Metastable Behavior on Cesium Fluoride-Treated Cu(In $_{1-x}$,Ga $_x$)Se $_2$ Solar Cells," *Phys. Status Solidi RRL – Rapid Res. Lett.*, vol. 14, no. 4, p. 1900701, Apr. 2020, doi: 10.1002/pssr.201900701.

[12] C. Walkons *et al.*, "Behavior of Na and RbF-Treated CdS/Cu(In,Ga)Se $_2$ Solar Cells with Stress Testing under Heat, Light, and Junction Bias," *Phys. Status Solidi RRL – Rapid Res. Lett.*, vol. 15, no. 2, p. 2000530, Feb. 2021, doi: 10.1002/pssr.202000530.

[13] K. Bakker, H. N. Åhman, T. Burgers, N. Barreau, A. Weeber, and M. Theelen, "Propagation mechanism of reverse bias induced defects in Cu(In,Ga)Se2 solar

cells," *Sol. Energy Mater. Sol. Cells*, vol. 205, p. 110249, Feb. 2020, doi: 10.1016/j.solmat.2019.110249.

[14] S. Nofal and B. E. Pieters, "A novel non-destructive characterization method to investigate hot-spot formation in CIGS solar cells using lock-in thermography," in *Conference Record of the IEEE Photovoltaic Specialists Conference*, 2021, pp. 1328–1330. doi: 10.1109/PVSC43889.2021.9518804.

[15] P. Yilmaz, J. Schmitz, and M. Theelen, "Potential induced degradation of CIGS PV systems: A literature review," *Renew. Sustain. Energy Rev.*, vol. 154, p. 111819, Feb. 2022, doi: 10.1016/j.rser.2021.111819.

[16] S. Lee *et al.*, "Characterization of Potential-Induced Degradation and Recovery in CIGS Solar Cells," *Energies*, vol. 14, no. 15, p. 4628, Jul. 2021, doi: 10.3390/en14154628.

[17] L. M. Mansfield, C. P. Muzzillo, S. Glynn, and I. L. Repins, "Cell-level reliability testing procedures for CIGS photovoltaics," *MRS Adv.*, vol. 6, no. 24, pp. 599–608, Sep. 2021, doi: 10.1557/s43580-021-00107-z.

[18] T. Kato, "Cu(In,Ga)(Se,S) $_2$ solar cell research in Solar Frontier: Progress and current status," *Jpn. J. Appl. Phys.*, vol. 56, no. 4S, p. 04CA02, Apr. 2017, doi: 10.7567/JJAP.56.04CA02.

[19] C. P. Muzzillo, H. M. Tong, and T. Anderson, "Chemistry of K in Cu(In,Ga)Se2 photovoltaic absorbers: Effects of temperature on Cu-K-In-Se films," *J. Alloys Compd.*, vol. 726, pp. 538–546, Dec. 2017, doi: 10.1016/j.jallcom.2017.08.019.

[20] I. L. Repins, S. Harvey, K. Bowers, S. Glynn, and L. M. Mansfield, "Predicting Ga and Cu Profiles in Co-Evaporated Cu(In,Ga)Se2 Using Modified Diffusion Equations and a Spreadsheet," *MRS Adv.*, vol. 2, no. 53, pp. 3169–3174, Nov. 2017, doi: 10.1557/adv.2017.350.

[21] C. P. Muzzillo, J. D. Poplawsky, H. M. Tong, W. Guo, and T. Anderson, "Revealing the beneficial role of K in grain interiors, grain boundaries, and at the buffer interface for highly efficient CuInSe $_2$ solar cells," *Prog. Photovolt. Res. Appl.*, vol. 26, no. 10, pp. 825–834, Oct. 2018, doi: 10.1002/pip.3022.

[22] C. P. Muzzillo, S. Glynn, G. Teeter, and L. M. Mansfield, "K, Rb, and Cs improve Cu(In,Ga)Se2 surface band alignment through reconstruction".

[23] L. M. Mansfield *et al.*, "Setting boundaries on the recipe for a successful RbF post-deposition treatment of CIGS," *Submitt. Sol. Energy Mater. Sol. Cells*.

[24] I. Repins *et al.*, "Large metastability in Cu (In,Ga)Se $_2$ devices: The importance of buffer properties," *Prog. Photovolt. Res. Appl.*, vol. 27, no. 9, pp. 749–759, Sep. 2019, doi: 10.1002/pip.3145.

[25] I. Repins, S. Glynn, K. Bowers, B. Stevens, C. L. Perkins, and L. Mansfield, "Using hole injection layers for decreased metastability and higher performance in Cu(In,Ga)Se2 devices," *Sol. Energy Mater. Sol. Cells*, vol. 215, p. 110597, Sep. 2020, doi: 10.1016/j.solmat.2020.110597.

[26] C. P. Muzzillo *et al.*, "Potential-Induced Degradation Depends on Leakage Current and Light/Electrical Bias in Cu(In,Ga)Se $_2$ Devices," *IEEE J. Photovolt.*, vol. 9, no. 6, pp. 1852–1856, Nov. 2019, doi: 10.1109/JPHOTOV.2019.2933189.

[27] C. P. Muzzillo *et al.*, "Potential-induced degradation of Cu(In,Ga)Se2 can occur by shunting the front i-ZnO and by damaging the p-n junction," *Sol. Energy*, vol. 232, pp. 298–303, Jan. 2022, doi: 10.1016/j.solener.2021.12.074.

THIS PAGE IS INTENTIONALLY LEFT BLANK.